23rd International Congress on Sound & Vibration
Athens, Greece 10-14 July 2016
ICSV23

PROPAGATION VELOCITY OF INERTIAL WAVES IN CYLINDRICAL SWIRLING FLOW

Alp Albayrak and Wolfgang Polifke
Professur für Thermofluiddynamik, Technische Universität München,
Boltzmannstr. 15, D-85748 Garching, Germany

email: albayrak@tfd.mw.tum.de

Inertial waves are observed in swirl burners, due to the acoustic waves crossing the swirl generators. These waves can significantly modify the flame response in terms of flame transfer function because the propagation mechanisms are different for acoustic and inertial waves. Acoustic waves propagate at the speed of sound, whereas inertial waves travel with convection. Small changes in burner configuration may convert the constructive superposition of flame responses to a destructive one, or vice versa, which may change the flame transfer function. Therefore, it is necessary to identify the propagation mechanisms correctly. The aim of this paper is to re-examine the assumption that inertial waves travel with convection. An analytical approach is combined with numerical simulations to determine and validate the propagation speed with emphasis on the impact of different swirl strengths.

1. Introduction

Lower emission of pollutants in gas turbines requires leaner fuel mixture for combustion process. This increases the likelihood of occurrence of combustion instability, which is caused by a feedback mechanism between acoustic waves and heat release rate fluctuations from the flame. In order to design safer and more reliable gas turbines, it is necessary to investigate the interaction between acoustic/hydrodynamic perturbation and flame dynamics.

Swirl burners are ubiquitous in combustion technology, because swirl promotes fuel/air mixing and flame stabilization. This work focuses on inertial waves generated by acoustic waves that propagate across the swirl generator. Inertial waves are understood to have a significant impact on the dynamic response of swirl flames to flow perturbations.

Richards and co-workers [1, 2, 3] studied the effects of the swirl vane location on thermo-acoustic stability. The sensitivity of the flame was credited to the phase lag between pressure and heat release rate. A convective time lag model is introduced for the tangential velocity perturbations that are generated at the swirler and propagate towards the flame front. In other words, overall flame response is the superposition of responses to tangential velocity and acoustic perturbations.

Komarek and Polifke [4] confirmed this scenario and showed individual Flame Transfer Functions (FTF) for the swirl waves and the acoustic axial velocity perturbations at burner mouth. The phase difference between these FTFs is then used to investigate how strongly constructive / destructive superposition can strongly modulate the gain of the overall FTF. Palies *et al.* [5, 6] modeled the generation and the propagation of these waves by the actuator disk theory by Cumpsty and Marble [7], where the tangential velocity perturbations are assumed to travel with convection. Kim and Santavicca [8] also confirmed the interference mechanism by FTF measurements.

However, it was noted already by Straub and Richards [3] that the convective time lag model leads to poor agreement against experiments. Similarly, Polifke and co-workers [4, 9] argued that the propagation speed of the swirl (inertial) waves differs from the convective speed.

The convective propagation assumption is scrutinized in this paper. Kerrebrock [10], Golubev and Atassi [11], and Tam and Auriault [12] investigated the interaction mechanism between the acoustic and inertial waves using space–time Fourier transformed linearized compressible Euler equations. They found non-convective behavior of the inertial waves, which is not influenced strongly by the compressibility in the range of Mach number 0.3.

In this work, an analytical expression for the inertial wave propagation is proposed by neglecting the compressibility. Using space–time Fourier transformed linearized incompressible Euler equations, an analytical description of the inertial wave propagation is proposed. Distinct modes appear, since the inertial waves are dispersed. These distinct modes propagate faster and slower than the convective speed. It is shown that the strength of the swirl affects the deviation from the convection. The analytical approach is then validated against the CFD simulations using OpenFOAM.

In Sec. 2.1, the space–time Fourier transform is applied to advection equation. The same approach is then applied to linearized Euler equations in Sec. 2.2 to investigate the inertial wave propagation. In Sec. 3 a simple example is shown for a solid body rotation in a duct, where the inertial wave propagation is quantified by a transfer function. Finally, in Sec. 4 the approach is validated against CFD simulations with a non-linear incompressible Navier-Stokes solver by OpenFoam.

2. Theory

The cylindrical swirling flows in most burners are incompressible. The interaction between acoustic and hydrodynamic waves is negligible and both can be investigated separately. Linearized incompressible Euler equations are employed in this work to describe the inertial wave propagation.

For all derivations there are common assumptions, i.e. the mean radial velocity being zero $\bar{u}_r = 0$, the mean axial velocity being uniform $\bar{u}_z\left(r\right) = \bar{u}_z$, the flow being axisymmetric $\partial\left(.\right)/\partial\theta$ and developed $\partial\left(.\right)/\partial z$.

The theory section is divided into two. In the first subsection, the assumption of the convective propagation mechanism for tangential velocity perturbations is revisited. The space–time Fourier transform is applied to advection equation. The propagation is quantified by a transfer function between the area averaged perturbations sampled at the upstream and downstream locations. In the second subsection, same approach is applied to linearized Euler equations that govern inertial waves.

2.1 Propagation of convective perturbations

The axisymmetric linearized advection equation for the tangential velocity perturbations u'_θ reads as

$$\frac{\partial u'_\theta}{\partial t} + \bar{u}_z \frac{\partial u'_\theta}{\partial z} = 0 \,, \tag{1}$$

where $(.)'$ denotes perturbed and $(\bar{.})$ mean quantities, u is velocity and (z, r, θ, t) are axial, radial and tangential coordinates and time, respectively.

Although this equation can directly be solved in time domain, the space–time Fourier transformation $(.)' = (\hat{.})\exp(-i\omega t + ikz)$ is performed in order to be consistent with Sec. 2.2. This transformation leads to an algebraic equation as dispersion relation $D\left(k, \omega\right) = 0$ that reads as

$$k\left(\omega\right) = \omega/\bar{u}_z, \tag{2}$$

where ω is the angular frequency and k is the axial wave-number. The perturbation in space–time

domain can be reconstructed by inverse Fourier transform as

$$u'_\theta(z,t) = \int_{-\infty}^{\infty} \left[\sum_{n=1}^{N} \hat{u}_\theta \exp\left(ik_n(\omega)\, z \right) \right] \exp(-i\omega t)\, \mathrm{d}\omega \,, \tag{3}$$

where N is the number of characteristic waves resulting from dispersion relation. For the advection equation there is only one characteristic wave $N = 1$ with convective phase speed $c_p = w/k = \bar{u}_z$.

A transfer function $T(\omega)$ can be introduced to quantify the propagation. The area averaged tangential velocity perturbation is measured at particular upstream 'z_u' and downstream 'z_d' positions and used as input and output, respectively. The transfer function reads

$$T(\omega) = \frac{\int_0^{r_o} 2\pi r \left[\sum_{n=1}^{N} \hat{u}_{\theta,n} \exp(ik_n z_d) \right] \mathrm{d}r}{\int_0^{r_o} 2\pi r \left[\sum_{n=1}^{N} \hat{u}_{\theta,n} \exp(ik_n z_u) \right] \mathrm{d}r} \,. \tag{4}$$

The input plane is chosen as $z_u = 0$ without loss of generality. The transfer function for the advection equation can be written as

$$T(\omega) = \exp\left(\frac{i\omega z_d}{\bar{u}_z} \right) \,, \tag{5}$$

whose gain and phase are $|T(\omega)| = 1$ and $\angle T(\omega) = \omega z_d / \bar{u}_z$, respectively (see Fig. 2 in Sec. 3).

2.2 Propagation of inertial waves

The linearized Euler equations in cylindrical coordinates read as

$$\frac{u'_r}{r} + \frac{\partial u'_r}{\partial r} + \frac{\partial u'_z}{\partial z} = 0 \,, \tag{6}$$

$$\frac{\partial u'_z}{\partial t} + \bar{u}_z \frac{\partial u'_z}{\partial z} + u'_r \frac{\partial \bar{u}_z}{\partial r} = -\frac{1}{\rho} \frac{\partial p'}{\partial z} \,, \tag{7}$$

$$\frac{\partial u'_r}{\partial t} + \bar{u}_z \frac{\partial u'_r}{\partial z} - \frac{2\bar{u}_\theta u'_\theta}{r} = -\frac{1}{\rho} \frac{\partial p'}{\partial r} \,, \tag{8}$$

$$\frac{\partial u'_\theta}{\partial t} + \bar{u}_z \frac{\partial u'_\theta}{\partial z} + u'_r \frac{\partial \bar{u}_\theta}{\partial r} + \frac{u'_r \bar{u}_\theta}{r} = 0 \,, \tag{9}$$

where p is pressure. Other variables are defined in Sec. 2.1. Space–time Fourier transformed equations can be written as a second order ODE for $\hat{u}_r$ as

$$\frac{d^2 \hat{u}_r}{dr^2} + \frac{1}{r} \frac{d\hat{u}_r}{dr} - \hat{u}_r \left(\frac{1}{r^2} + k^2 - \frac{2k^2 \bar{u}_\theta}{(w - \bar{u}_z k)^2 r^2} \frac{\partial(\bar{u}_\theta r)}{\partial r} \right) = 0 \,. \tag{10}$$

This equation requires prescribed mean tangential velocity $\bar{u}_\theta(r)$. For particular cases such as solid body rotation $\bar{u}_\theta(r) = Kr$, free vortex $\bar{u}_\theta(r) = K/r$ or uniform tangential velocity $\bar{u}_\theta(r) = K$, the analytical solution can be found.

Two boundary conditions are required for $\hat{u}_r(r)$, which define the dispersion relation $D(k,\omega) = 0$. The phase speed c_p corresponds to the propagation speed of the inertial waves. The propagation can be quantified by the transfer function defined in Eq. (4).

3. Illustrative example: Solid body rotation in a duct

For the ease of illustration, the analysis is carried out for a duct with radius of $r_o = 5$ mm. The uniform constant axial velocity profile is used $\bar{u}_z = 10$ m/s. The tangential velocity is prescribed as a solid body rotation $\bar{u}_\theta(r) = Kr$, where $K = 2000$ s^{-1}. The corresponding Reynolds Number is $Re = 6667$ lying in turbulent regime.

The symmetry condition at center is translated to a boundary condition $\hat{u}_r(0) = 0$. Second boundary condition $\hat{u}_r(r_o) = 0$ is from the impermeability condition at duct wall. The analytical solution reads as

$$\hat{u}_{\theta,n}(r) = c_n J_1(A_n r) + d_n Y_1(A_n r) \ , \tag{11}$$

$$\hat{u}_{r,n}(r) = \frac{\bar{u}_z k_n - \omega}{2Ki} \left[c_n J_1(A_n r) + d_n Y_1(A_n r)\right] \ , \tag{12}$$

$$\hat{u}_{z,n}(r) = \frac{A_n(\bar{u}_z k_n - \omega)}{2Kk_n} \left[c_n J_0(A_n r) + d_n Y_0(A_n r)\right] \ , \tag{13}$$

$$\hat{p}_n(r) = -\frac{A_n(\bar{u}_z k_n - \omega)^2 \rho}{2Kk_n^2} \left[c_n J_0(A_n r) + d_n Y_0(A_n r)\right] \ , \tag{14}$$

where $A_n = k_n\sqrt{4K^2 - (\bar{u}_z k_n - \omega)^2}/(\bar{u}_z k_n - \omega)$ and J and Y are the Bessel functions of first and second kind, respectively. J and Y are orthogonal functions, which form complete solution.

Since Y_1 goes to infinity at $r = 0$, the boundary condition $\hat{u}_r(0) = 0$ cannot be satisfied unless the coefficients of Y vanish $d_n = 0$. Applying the second boundary condition $\hat{u}_r(r_o) = 0$, the dispersion relation $D(k, \omega)$ can be formed as

$$J_1(A_n r_o) = 0 \Rightarrow A_n r_o = j_n \ , \forall n \in \mathbb{N}^+ \ , \tag{15}$$

where j_n are the roots of Bessel function of first kind J_1. Axial wave-numbers $k_n(\omega)$ can be determined explicitly by solving fourth order polynomial. This indicates that for each n there exist four axial wave-numbers that have the same mode shape. Two of them propagate upstream while one grows and the other decays, which are assumed to be unphysical (see Sec. 3.1).

Other two waves are addressed as inertial waves and propagate downstream (neither growing nor decaying) at different speeds, one is faster '$+$' and the other is slower '$-$' than the convection. In left part of Fig. 1, the dispersion relation defined in Eq. (15) is represented. Roots indicate eigenvalues as axial wave-numbers, where x-axis is the normalized phase velocity $c_p^* = \omega/(k\bar{u}_z)$.

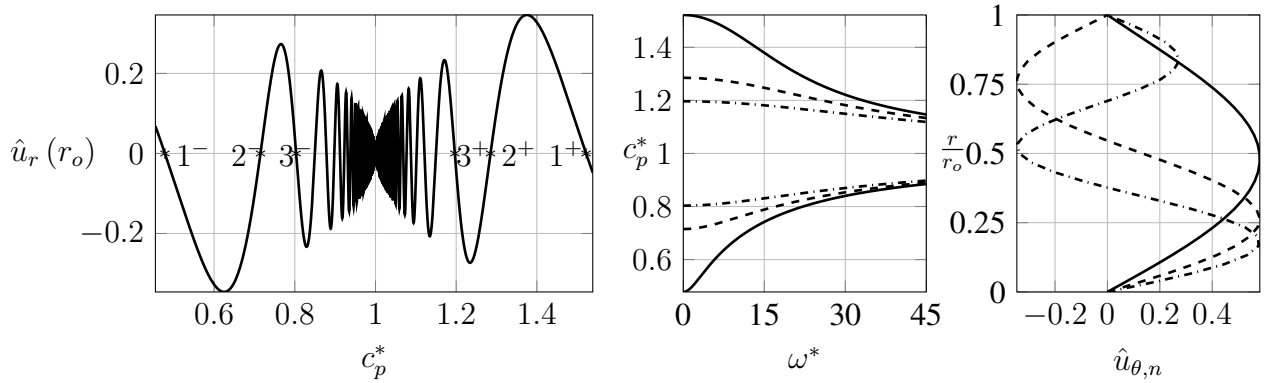

Figure 1: Left: Second boundary condition $\hat{u}_{r,n}(r_0) = 0$ as a function of normalized phase speed $c_p^* = \omega/(k\bar{u}_z)$ for $\omega = 100$ rad/s, $U_z = 10$ m/s, $K = 2000$ s^{-1} and $r_o = 5$ mm. Zeros corresponds to the eigenvalues: '$+$' and '$-$' indicating faster and slower waves than convection $c_p^* = 1$, respectively. Middle: Normalized phase speeds for the first three modes including both '$+$' and '$-$' as a function of normalized angular frequency $\omega^* = \omega z_d/\bar{u}_z$. Right: The eigenvectors of tangential velocity perturbation component $\hat{u}_{\theta,n}$ for the first three slower '$-$' modes. $n = 1$ (——), $n = 2$ (- · - · -), $n = 3$ (- - -).

The normalized phase speed can be written explicitly as

$$c^*_{p,n} = 1 \pm \frac{2K}{\bar{u}_z} \frac{r_o}{\sqrt{k^2 r_o^2 + j_n^2}} \,, \tag{16}$$

which shows the effect of the circulation strength K on the propagation of inertial waves. As circulation strength increases, the deviation from convection increases too. The normalized phase speed as a function of normalized angular frequency $\omega^* = \omega z_d / \bar{u}_z$ for the first three modes $n = 1, 2, 3$ is shown in the middle part of Fig. 1. As n increases, the phase speed approaches the convective speed. Moreover, the phase speed depends on the angular frequency. At low frequencies the propagation deviates from the convection the most. For high frequencies, both fast '$+$' and slow '$-$' propagation speeds approach the convection. Additionally, the inertial waves are not only perturbations in tangential velocity, but also in radial and axial directions. This is evident from Eqs. (11), (12) and (13).

The eigenvectors of the tangential velocity perturbation component $\hat{u}_{\theta,n}$ related to three outermost slower waves '$-$' are illustrated in the right part of Fig. 1 as a function of radius. Although the modes corresponding to the faster waves '$+$' are not plotted, they are equal to the negative of the slower wave modes. As n increases, the modes become more oscillatory.

3.1 Construction of boundary condition regarding number of characteristics

Linearized compressible Euler equations for perfect gas can be described by five field variables $[\rho', p', u'_z, u'_r, u'_\theta]$ and corresponding five transport equations. Related to the transport equations there are five characteristic waves, namely two acoustic waves (propagating downstream and upstream), the convective entropy wave and two inertial waves. The latter are studied in this paper.

Assuming the flow is incompressible, the energy equation is decoupled from the system of equations and therefore, the entropy wave is eliminated. The incompressible system is described by four field variables $[u'_z, u'_r, u'_\theta, p']$ and four partial differential equations. The type of pressure equation changes from hyperbolic to elliptic. The non-local behavior of the elliptic equation modifies the nature of the acoustic waves making their propagation speed infinite. The incompressible equations have, therefore, only two inertial waves as characteristics, which contradicts Eq. (15) that has four characteristics. In this paper, the upward propagating waves are postulated to be unphysical and related to modified spurious acoustic waves.

In order to construct a well-posed problem, the boundary condition at inlet $z = 0$ should be defined for each variable $[u'_z, u'_r, u'_\theta, p']$. As there exist only two characteristics, the variables cannot be chosen freely, otherwise non-local waves (spurious acoustic waves) are triggered, which cannot be described as space–time Fourier transform. However, in order to be consistent with the actuator disk theory [5, 6, 7], a perturbation in tangential velocity $\hat{u}_\theta = f_\theta(r)$ is imposed. Other components of the velocity perturbation are set to zero and the pressure perturbation is set as Neumann boundary condition.

For simplicity, the tangential velocity perturbation at the inlet is assumed as the first mode shape $f_\theta(r) = J_1(j_1 r / r_o)$ shown with solid line in the right part of Fig. 1. Since Bessel functions form an orthogonal basis, the modes other than $n = 1$ are not excited. In this case, the coefficients are calculated as the following set of equations for $\hat{u}_\theta, \hat{u}_r, \hat{u}_z$ respectively

$$1 = -c_{1_+} + c_{1_-} + c_{1_u} \,, \tag{17}$$

$$0 = -\frac{\bar{u}_z k_{1_+} - \omega}{2Ki} c_{1_+} + \frac{\bar{u}_z k_{1_-} - \omega}{2Ki} c_{1_-} + \frac{\bar{u}_z k_{1_u} - \omega}{2Ki} c_{1_u} \,, \tag{18}$$

$$0 = \frac{A_{1_+}(\bar{u}_z k_{1_+} - \omega)}{2K k_{1_+}} c_{1_+} + \frac{A_{1_-}(\bar{u}_z k_{1_-} - \omega)}{2K k_{1_-}} c_{1_-} + \frac{A_{1_u}(\bar{u}_z k_{1_u} - \omega)}{2K k_{1_u}} c_{1_u} \,, \tag{19}$$

where subscript "u" stands for the upward propagating growing wave. The upward propagating decaying wave is neglected, because in downstream direction, it acts as if the wave is growing, which

ruins the transfer function. Since three characteristics are used for construction of perturbation, the pressure boundary condition is neglected too. The resulting coefficients are frequency dependent and can be approximated by $c_{1+} \approx -0.5$, $c_{1-} \approx 0.5$ and $c_{1u} \approx 0$. It is straightforward to construct any type of perturbation similarly, which can be expressed as a summation of Bessel function of first kind J_1.

The perturbation in space–time domain at a downstream location can be constructed by considering only inertial waves

$$u'_\theta(z,r,t) = J_1\left(j_1\frac{r}{r_o}\right)\int_{-\infty}^{\infty}\Big[-c_{1+}\exp\left(ik_{1+}z\right)+c_{1-}\exp\left(ik_{1-}z\right)\Big]\exp\left(-i\omega t\right)\mathrm{d}\omega\ . \tag{20}$$

3.2 Derivation of transfer function

The transfer function defined in Eq. (4) can be simplified as

$$T(\omega) = -c_{1+}\exp\left(ik_{1+}z_d\right)+c_{1-}\exp\left(ik_{1-}z_d\right)\ . \tag{21}$$

In Fig. 2 the gain and the phase are plotted at downstream position $z_d = 3r_o = 15$mm with the solid line (——) and compared against the convective model with the dashed line (- - -). The CFD results are indicated with the (◦) symbol and explained in Sec. 4. In the first two columns, the slow and fast modes are analyzed separately. Each mode independently shows a constant gain $|T(\omega)| = 1$ and a phase deviating from the convective phase as expected. For fast mode, the phase is steeper than the convection at low frequencies and becomes parallel for higher frequencies. This agrees well with phase speeds shown in the middle part of Fig. 1, where the phase speeds approach the convective speed as frequency increases. The similar arguments can be made for the slow mode. The complete inertial wave propagation is described by the superposition of the two modes as shown in the third column. The constructive superposition results in gain values around $|T(\omega)| \approx 1$ and the destructive superposition results around $|T(\omega)| \approx 0$. The superposition in the phase results in almost convective phase. This might be misleading, since the propagation is far from being convective.

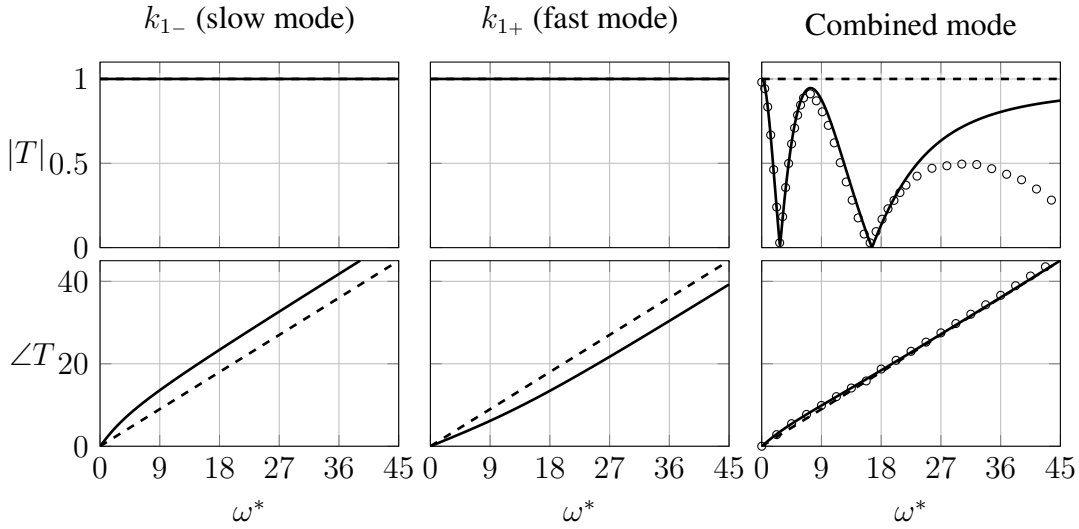

Figure 2: Comparison of the Bode plots for inertial wave (——), convective wave (- - -) and CFD results (◦). First two columns show slower k_1^- and faster k_1^+ modes, respectively and the third column shows the combined mode.

The Fig. 3 shows the gain plots $|T(\omega)|$ for output locations, $z_d = 3r_o = 15$ mm and $z_d = 6r_o = 30$ mm. As the downstream position z_d increases, more destructive superpositions exist and the frequencies shift. This characteristic of inertial waves is very crucial for experiments and CFD simulations of real swirl generators, where the source of the inertial wave is not well known. Since

the tangential velocity perturbations measured at upstream location z_u is the denominator in Transfer Function $T(\omega)$, a destructive superposition results in $T(\omega) \to \infty$. This behavior is not observed in the case presented in this paper, because the upstream reference position is located at inlet $z_u = 0$, where the perturbations are generated and there is no possibility for destructive superposition.

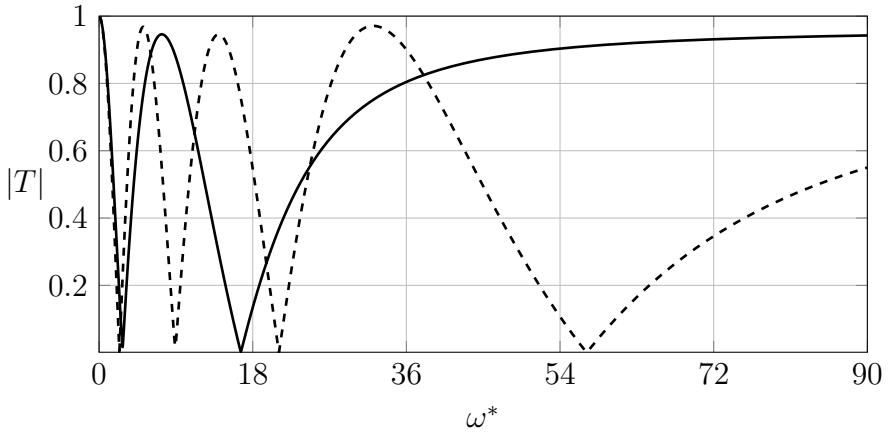

Figure 3: Gain plot for $z_d = 3r_o = 15$mm (——) and $z_d = 6r_o = 30$mm (- - -).

4. Comparison against CFD results

The CFD simulations are performed for the same configuration as described in Sec. 3 using OpenFOAM. The transient incompressible Navier-Stokes equations are solved using PIMPLE algorithm. The slip wall boundary conditions are used to match the inviscid analytical approach. The tangential velocity perturbations are generated at the inlet boundary condition by broad-band excitation. Then, the transfer function is constructed by Wiener-Hopf inversion [13].

As shown in Fig. 2, a good agreement is achieved between CFD results and analytical model for the low and moderate frequencies. For high frequencies, the CFD simulations show low pass behavior due to the viscous dissipation, which is not present in the analytical approach. However, very high frequencies are not relevant for the linear combustion dynamics. Therefore, those frequencies can be neglected and reliable results can still be obtained.

5. Conclusion

In order to investigate the inertial wave propagation, space–time Fourier transformation is applied to linearized incompressible Euler equations. The transformed equations are solved analytically as a second order ODE, where infinite number of waves with phase speeds diverging from convection are revealed. It is shown that the phase speed of the inertial waves depends on mean tangential velocity. As mean tangential velocity increases, the deviation from convection increases too. By defining a transfer function between tangential velocity perturbations at different locations, the inertial wave propagation is compared against the convective propagation by considering a solid body rotation in a duct. The analytical model is successfully validated against numerical simulations. The model can be coupled with low order models for more reliable estimation of thermo-acoustic stability. It is also possible to build a velocity perturbation model that can be used to study the impact of inertial waves on the flame dynamics.

Acknowledgments

The presented work is part of the Marie Curie Initial Training Network Thermo-acoustic and aero-acoustic nonlinearities in green combustors with orifice structures (TANGO). We gratefully acknowledge the financial support from the European Commission under call FP7-PEOPLE-ITN-2012.

REFERENCES

1. Richards, G. A. and Yip, M. Oscillating combustion from a premix fuel nozzle, *The Combustion Institute/ American Flame Research Committee Meeting, San Antonio, TX (United States)*, (1995).

2. Straub, D. L., Richards, G. A., Yip, M. J., Rogers, W. A. and Robey, E. H. Importance of axial swirl vane location on combustion dynamics for lean premix fuel injectors, *34th AIAA/ASME/SAE/ASEE Joint Propulsion Conference and Exhibit*, Cleveland, OH, USA, Jul., (1998).

3. Straub, D. L. and Richards, G. A. Effect of axial swirl vane location on combustion dynamics, *ASME 1999 International Gas Turbine and Aeroengine Congress and Exhibition*, pp. V002T02A014–V002T02A014, American Society of Mechanical Engineers, (1999).

4. Komarek, T. and Polifke, W. Impact of Swirl Fluctuations on the Flame Response of a Perfectly Premixed Swirl Burner, *Journal of Engineering for Gas Turbines and Power*, **132** (6), 061503–1,7, (2010).

5. Palies, P., Durox, D., Schuller, T. and Candel, S. The combined dynamics of swirler and turbulent premixed swirling flames, *Combustion and Flame*, **157**, 1698–1717, (2010).

6. Palies, P., Schuller, T., Durox, D. and Candel, S. Modeling of premixed swirling flames transfer functions, *Proceedings of the Combustion Institute*, **33** (2), 2967 – 2974, (2011).

7. Cumpsty, N. and Marble, F. The interaction of entropy fluctuations with turbine blade rows; a mechanism of turbojet engine noise, *Proceedings of the Royal Society of London A: Mathematical, Physical and Engineering Sciences*, vol. 357, pp. 323–344, The Royal Society, (1977).

8. Kim, K. T. and Santavicca, D. A. Interference mechanisms of acoustic/convective disturbances in a swirl-stabilized lean-premixed combustor, *Combustion and Flame*, **160** (8), 1441–1457, (2013).

9. Tay-Wo-Chong, L., Komarek, T., Kaess, R., Föller, S. and Polifke, W. Identification of flame transfer functions from LES of a premixed swirl burner, *Proceedings of ASME Turbo Expo 2010*, Glasgow, UK, Jun., GT2010-22769, ASME, (2010).

10. Kerrebrock, J. L. Small disturbances in turbomachine annuli with swirl, *AIAA Journal*, **15** (6), 794–803, (1977).

11. Golubev, V. V. and Atassi, H. M. Acoustic-Vorticity Waves in Swirling Flows, *Journal of Sound and Vibration*, **209** (2), 203–222, (1998).

12. Tam, C. K. and Auriault, L. The wave modes in ducted swirling flows, *Journal of Fluid Mechanics*, **371**, 1–20, (1998).

13. Polifke, W. Black-box system identification for reduced order model construction, *Annals of Nuclear Energy*, **67C**, 109–128, (2014).